

Aerostructural wing optimization of a regional jet considering mission fuel burn

Nicolas P. Bons
Joaquim R. R. A. Martins¹

Department of Aerospace Engineering
University of Michigan, Ann Arbor

Felipe I. K. Odaguil
Ana P. C. Cuco

Embraer, São José dos Campos
São Paulo, Brazil

High-fidelity multidisciplinary design optimization (MDO) promises rigorous balancing of the multidisciplinary trade-offs inherent to aircraft wings. However, collaborations between academia and industry rarely put MDO to the test on practical design problems. In this work, MDO is applied to the design of a regional jet wing to minimize fuel burn. High-fidelity aerostructural analysis is used to model the wing and capture trade-offs between structural weight and aerodynamic performance. A novel approach is used to calculate fuel burn for climb and descent using a low-fidelity model, improving the relevancy of the optimization results for short-haul missions. A wing-only geometry is used to explore the design space and generate a series of Pareto fronts for different geometric parametrizations. Finally, an aerostructural optimization is conducted with a complete wing-body-tail geometry of an Embraer regional jet. The optimizer increases the wingspan and decreases the sweep of the original wing to achieve a 3.6% decrease in fuel burn.

Keywords: aircraft design, aerostructural optimization, computational fluid dynamics

1 Introduction

Traditionally, a wing's planform, airfoil shape, and structure are designed separately. One of the first steps is determining the area and basic shape of the wing planform that will support the mission requirements. Historical data and low-fidelity models can rapidly obtain this basic wing definition. Eventually, the in-flight wing shape is designed by aerodynamicists to achieve the desired performance. It is then the job of structural engineers to design a jig shape and structure that will revert to the flying shape when deformed aeroelastically in flight. The wing design is then transferred back and forth between the aerodynamics and structures groups to converge on the lightest wing that can satisfy performance requirements. While this description is oversimplified, it highlights the separation between the design of the wing shape and structure. The complexity inherent to wing design has led to this segmented approach. Advances in computing power and numerical methods have enabled multidisciplinary design optimization (MDO) techniques. One of the aims of MDO is to remove artificial barriers in the design process that may have arisen in the past due to organizational practicalities. When the entire design can be robustly optimized simultaneously, it should be possible to converge to a better design with significantly reduced time and resources.

MDO of wings has been an active area of research for many years, especially with lower fidelity aerostructural models [1–6]. However, only recently has high-fidelity aerostructural wing optimization reached a level of maturity at which realistic wing design can be done [7,8]. Some examples include optimization of the Common Research Model (CRM) [9], the D8 [10], tow-steered composite wings [11,12], and the Aeron Supersonic AS2 [13].

Despite the work in the academic literature, competition in industry makes it difficult to determine to what extent these methods have been adopted and have borne fruit. To bridge this gap between industry and academia, we collaborated with Embraer to optimize the wing design of an authentic regional aircraft using the MDO of Aircraft Configurations with High fidelity (MACH) framework. This collaboration allows us to evaluate the benefit obtained by applying MDO in the industrial aircraft design process. The results herein compare the baseline wing to a wing with opti-

mized structural sizing, airfoil shape, and twist distribution. This comparison serves as a litmus test for the optimization problem—significant deviation from the baseline design would indicate a failure to capture the design requirements adequately. Then we extend the optimization problem to include planform variables, allowing the optimizer more freedom to trade between structural weight and aerodynamic performance. For each wing optimization problem, we model the aerodynamics of the full aircraft geometry, including fuselage, wing, and empennage. This way, subtle interactions between the wing and the rest of the geometry are not neglected, and we can ensure that the optimized design is properly trimmed. Additionally, we can experiment with sizing the horizontal stabilizer to account for changes in the wing planform.

In the spirit of practical wing design, choosing an objective function that suitably quantifies the aircraft's actual performance is essential. Fuel burn is often an objective function in wing design optimization problems because it represents a large proportion of the operating cost. Various methods exist for estimating fuel burn, each with assumptions and approximations influencing the optimization outcome. For example, the fuel burn calculation can be based on a single flow condition or aggregate information from multiple design points. However, using numerical optimization to design a wing for a single flight condition can have undesired consequences at off-design conditions [14]. A multipoint optimization problem, where the performance at multiple flight conditions is incorporated into the objective function, can produce a more robust design.

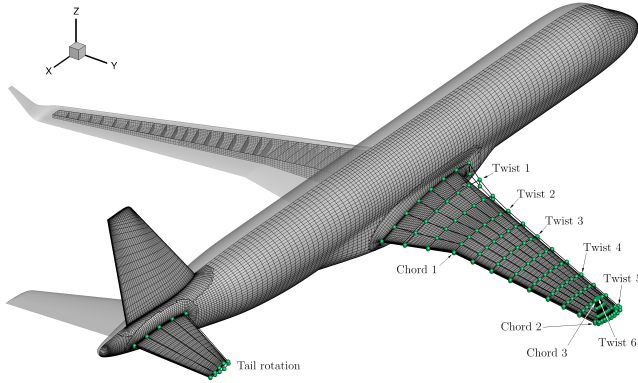
There are different ways to formulate a multipoint objective function. Commonly, the objective function is a weighted average of a figure of merit computed at each flight condition. However, the weighting significantly affects the result, and it is not always clear how to choose the weights a priori. Liem et al. [15] devised a method to calculate the weights for 25 different flight conditions to achieve minimum fuel burn for the CRM geometry. They generated a surrogate model of aerodynamic coefficients with aerostructural analyses of the baseline geometry and then calculated the fuel burn for hundreds of representative missions using the surrogate model. Finally, they computed the sensitivity of the total fuel burn with respect to each of the 25 flight conditions. They used this as the weight in the objective function for the aerostructural optimization. Not surprisingly, the aircraft optimized with this

¹Corresponding Author.

Version 1, August 31, 2022

Table 1 R-jet aircraft Specifications

Description	Symbol	Units	Value
Wingspan	b	m	28.72
Reference area	S	m ²	95.4
Aspect ratio	\mathcal{R}		8.6
Maximum takeoff weight	MTOW	kg	51,800
Operating empty weight	OEW	kg	27,900

**Fig. 1 Computational grids for the R-jet configuration.**

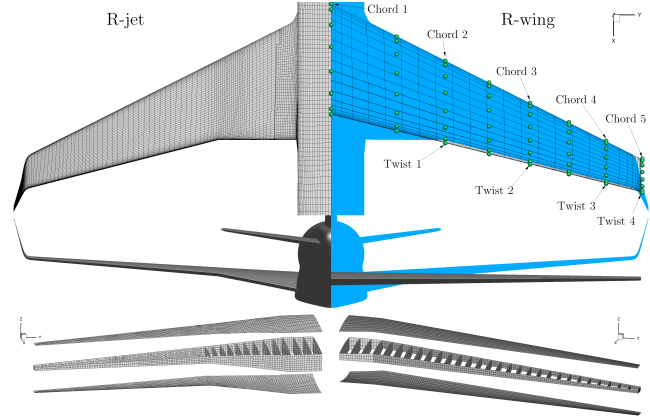
multi-mission objective function weighting performed much better than a single-point optimum when tested on the full spectrum of missions.

In the study just cited, all flight conditions included in the fuel burn aggregation were sampled from the cruise flight phase. The fuel burn in climb and descent is negligible for an aircraft that typically flies long-range missions. However, a regional aircraft regularly flies missions where the fuel used in climb and descent exceeds that used in cruise. Therefore, if fuel burn is the quantitative measure of aircraft performance, it is important to include design points from the climb and descent segments in the fuel burn aggregation. Liem et al. [16] addressed this concern in a paper similarly focused on regional aircraft design optimization. They optimized the mission profiles for two missions of varying ranges by integrating fuel burn across the climb, cruise, and descent segments. Then they used the optimized mission profiles to compute fuel burn while optimizing the aerostructural design of the aircraft wing. In the present work, we also use an integration scheme to account for the fuel burn in climb and descent. However, in contrast to Liem et al., we can include the fuel burn integration directly in the optimization by using a low-fidelity model to analyze the climb and descent design points. Furthermore, we take a closer look at how the design is impacted by considering full-mission fuel burn instead of only considering cruise.

2 Problem Description

2.1 Geometric Modeling. The specifications of the Embraer regional jet are provided in Table 1. Embraer furnished the CAD descriptions of the fuselage, wing, and empennage surfaces that define the outer mold line (OML). Each geometry component is meshed individually using structured hexahedral cells and then combined into a single overset mesh (Figure 1). The grid used for optimization has just over 2 million cells. The finite element model of the wingbox is based on a structural layout from Embraer. The wingbox mesh consists of 8,018 quadrilateral cells modeled as second-order mixed interpolation of tensorial components (MITC) shell elements. Together, the OML and wingbox form the baseline design of the aircraft, which has been designated R-jet for this study.

We also created a supplementary wing-only aircraft model called R-wing. This wing geometry has the same general specifications

**Fig. 2 Computational grids for the R-wing configuration juxtaposed with the R-jet grids.****Table 2 The R-wing mesh reduces the computational cost of aerostructural analysis by a factor of 1500 when compared with the R-jet overset mesh.**

Geometry	Cells	N Cores	Solution time	Adjoint time
R-jet	2,071,850	79	1261 s	587 s
R-wing	30,528	1	87 s	77 s

detailed in Table 1, but it differs from the R-jet in that it has an RAE-2822 cross-section, a straight trailing edge, and a conventional wingtip (as opposed to a winglet). The R-wing wingbox has the same basic layout as the R-jet, but the ribs are all aligned with the freestream. Table 2 shows the size of the R-wing computational fluid dynamics (CFD) mesh and the substantial reduction in computational expense when compared with the full R-jet overset mesh. The R-wing mesh reduces the proc-hours by 1500 and 1000 times for analysis and a single adjoint, respectively. The primary purpose for creating the R-wing geometry is to enable rapid optimization cycles for studying the effects of mission analysis on the optimized design. However, a side benefit of an inexpensive computational model is that it accelerates the inevitable troubleshooting process for a new optimization problem. Generally, optimizer parameters and scaling factors tuned on the simple model can be used with the more expensive model.

2.2 Mission Description. The objective of the design problem is to minimize the average fuel burn of three representative missions, weighted as follows:

$$\bar{W}_{\text{fuel}} = 0.5W_{\text{fuel,NOM}} + 0.2W_{\text{fuel,LR}} + 0.3W_{\text{fuel,HS}} \quad (1)$$

The details of the three missions can be found in Table 3. The weights in Equation 1 are related to the proportion of routes a regional jet typically flies at each range. The total fuel burn for each of these missions is the difference in weight from takeoff (W_0) to landing (W_5), where the basic mission profile is defined as indicated in Figure 3. It is expected that most of the fuel is burned in the climb and cruise segments and that the ratio of climb fuel burn to cruise fuel burn will decrease as the mission range increases. For instance, Liem et al. [16] found that the climb and cruise segments accounted for 32% and 26% of the total fuel burn for a 500 nm mission and 13% and 68% of the total for a 2000 nm mission. For aircraft that typically fly missions where the distance covered in the climb is small compared to the total mission range, the benefit of incorporating the climb segment into the total fuel burn objective is negligible. In such cases, it would still be essential to consider the flightworthiness requirements of the climb segment as constraints in the optimization problem. However, as

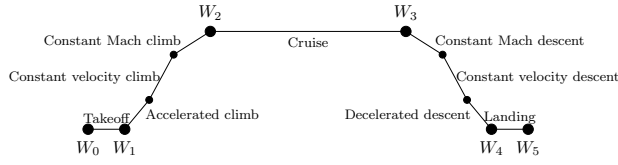


Fig. 3 Basic mission profile.

Table 3 Mission details

Code	Description	Range (nm)	Mach	Altitude (ft)	Payload (kg)
NOM	Nominal	600	0.78	36,000	10,000
LR	Long-range	1000	0.74	36,000	10,000
HS	High-speed	300	0.80	36,000	10,000

the ratio of climb range to cruise range increases, it becomes more important to consider the fuel burned during the climb, mainly because the fuel burn per mile is greater in climb than in cruise. To simplify the estimation of climb fuel burn, the hypothetical cruise fuel burn over the climb distance can be augmented with a climb fuel increment factor computed from empirical data sets [17].

3 Computational Framework

The MACH framework offers a powerful, automated approach to aircraft design [18]. The motivation for developing MACH is to enable efficient, high-fidelity, gradient-based, multidisciplinary optimization of aircraft. The most significant benefit of the MACH framework for optimization is that each module embedded in the optimization loop provides efficient, accurate gradient computation in addition to its primary function.

The component hierarchy and process flow for aerostructural optimization in the MACH framework are shown in the XDASM [19] diagram in Figure 4. The optimizer changes the design at each iteration, the MDA solver converges the aerostructural system, and functions of interest are returned to the optimizer. In this work, we use the optimizer SNOPT v7.7 [20] through the pyOptSparse Python interface [21].² The geometry is parametrized with a free-form deformation (FFD) scheme [22] implemented in pyGeo [23]. The FFD parametrization applies to the aerodynamic and structural meshes so that the wingbox is always consistent with the outer mold line (OML). Changes to the OML are propagated from the aerodynamic surface nodes to the volume mesh using the inverse-distance mesh warping algorithm in IDWarp [24].³ We obtain the solution of the aerostructural system with a Gauss–Seidel iterative scheme. ADflow [25,26] is used to obtain a Reynolds-averaged Navier–Stokes solution of the flow with the Spalart–Allmaras turbulence model. Toolkit for the Analysis of Composite Structures (TACS) [27] solves for the structure displacement under the aerodynamic loads. A Krylov method is used to solve the coupled adjoint of the multidisciplinary system. The structural node displacements and aerodynamic surface loads are transferred between the aerodynamic and structural meshes using a rigid link load and displacement transfer scheme first introduced by Brown [28] and subsequently described in the context of MACH [18,29]. In addition to the high-fidelity aerostructural analysis modules, we also include a module for mission analysis in the studies reported herein (see Section 3.3).

3.1 Aerodynamic Models. Both high-fidelity and low-fidelity aerodynamics models are used in the optimization problems presented in this work. The high-fidelity data are produced using the coupled aerostructural analysis described previously. To account

for the lack of fuselage and empennage in the R-wing configuration, we apply an additive drag markup of $D/q = 0.75 \text{ m}^2$ and a multiplicative lift markup of 1.05. With these markups included, the mission fuel burn computed for the R-wing configuration is similar to that of the R-jet configuration. The computational grids for the aerodynamics and structures are shown in Figure 1 for R-jet and Figure 2 for R-wing. By contrast, the conceptual-level formulas in pyConcept require only a few data points representing the basic shape of the wing geometry.

pyConcept is a module in the MACH framework that can be used to calculate geometric parameters such as reference area, mean aerodynamic chord, and sweep angle. The wing geometry is represented by points located along the leading and trailing edges and the location of maximum thickness on the baseline geometry. These points are extracted from the baseline wing airfoil slices and then embedded in the free-form deformation (FFD). Geometric parameters depend on the FFD design variables via the embedded points.

pyConcept also provides estimates of aerodynamic performance based on fundamental geometric properties. For instance, induced drag can be approximated as

$$C_{D,i} = \frac{C_L^2}{\pi Re}, \quad (2)$$

where both Re and e can be calculated solely from geometric properties and flow conditions. Similarly, parasitic drag is computed using the component buildup method suggested by Raymer [30], wherein the drag of each component is a function of the wetted area, the flat-plate skin friction coefficient, a form factor, and an interference factor. These estimates are not expected to yield accurate predictions but are intended to capture the trends due to changing geometric parameters. The novelty of this approach is that we can maintain the FFD parametrization as a means of adjusting the geometric parameters relevant to the conceptual formulas. Like everything else in the MACH framework, the fundamental philosophy in developing this capability was to allow for efficient, accurate derivative computation. The derivatives of the pyConcept functions with respect to the geometric parameters are analytically derived, and the derivatives of the geometric parameters with respect to the airfoil points are computed with the complex-step method. The derivatives of the points with respect to the design variables are already handled in pyGeo. In the end, derivatives of the pyConcept functions with respect to the design variables are obtained by combining the three different sets of gradients using the chain rule.

The required points are extracted from slices of the R-wing and R-jet wing surfaces. For a given cross-section slice, pyConcept uses points on the leading and trailing edges and a point on each of the upper and lower surfaces at the location of the maximum thickness (Figure 5). With these points, pyConcept can compute necessary quantities such as planform area, quarter-chord sweep, and the value and location of the mean aerodynamic chord (MAC). As already mentioned, these points are embedded in the FFD so that they are updated as the design changes during the optimization.

On the baseline configuration, the drag estimation from pyConcept matches well with the high-fidelity aerostructural result at the cruise flow condition (Figure 6). As the speed and altitude of the flow condition decrease, the low-fidelity analysis underestimates drag by as much as 20%. The difference between low-fidelity and high-fidelity analyses on an optimized design is less than or equal to that of the baseline design. In this instance, the terms high-fidelity and low-fidelity are used in a relative sense. The CFD mesh used for the R-wing analysis is relatively coarse and is only used to obtain rough estimates of aerodynamic performance. However, it does provide richer information than the pyConcept model.

3.2 Structural Model. TACS was developed by Kennedy and Martins [31] for the analysis and optimization of the thin-walled

²<https://github.com/mdolab/pyoptsparse>

³<https://github.com/mdolab/idwarp>

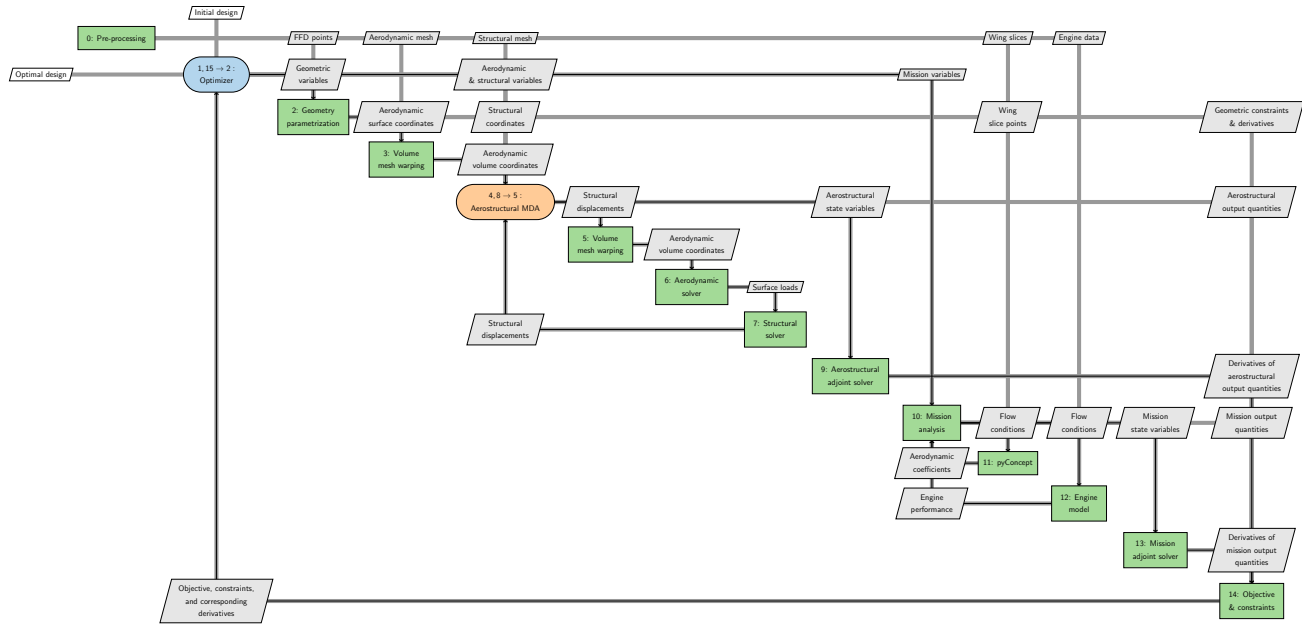


Fig. 4 XDSM diagram of aerostructural mission optimization with MACH.

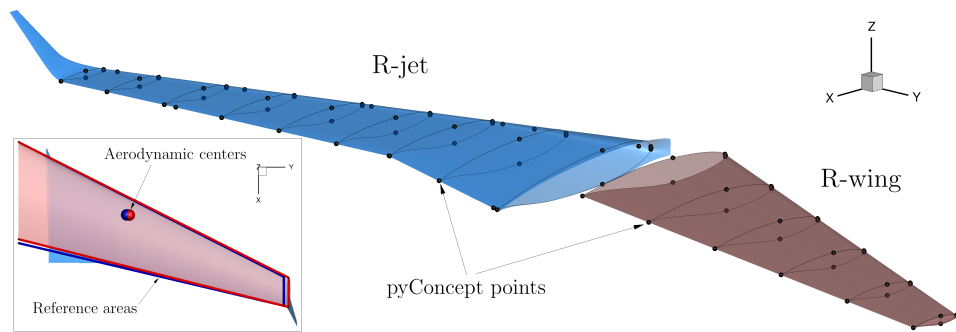


Fig. 5 Points are extracted from the R-wing and R-jet wings in order to create a basic representation of the geometry in pyConcept.

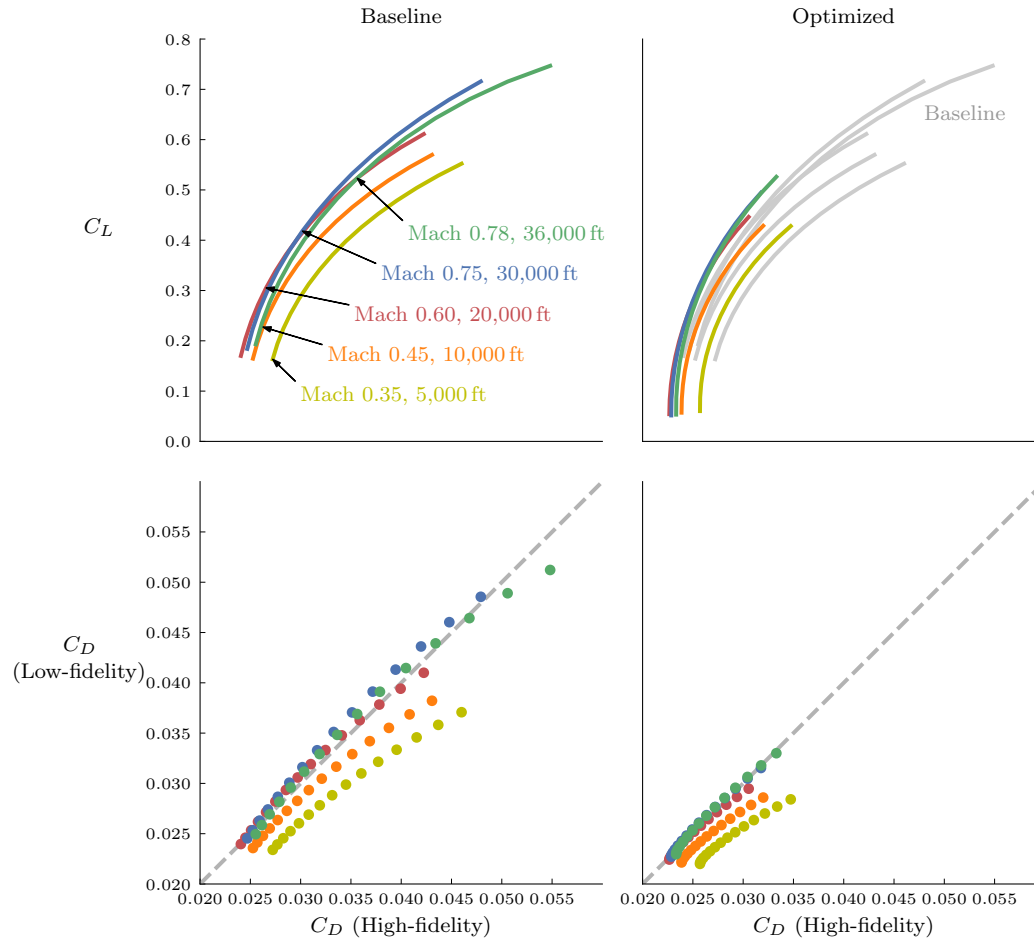


Fig. 6 On both baseline and optimized designs, the low-fidelity drag polar from pyConcept coincides with the high-fidelity aerostructural result at cruise flow conditions. The error in the low-fidelity method grows as the speed and altitude decrease.

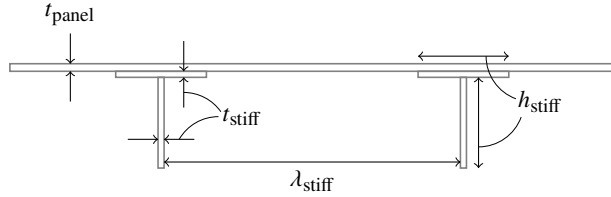


Fig. 7 Representative depiction of smeared stiffness model.

structures typical in aircraft. Typically, we analyze wingbox structures comprising ribs, spars, and skins. Each part of the structure is discretized with quadrilateral shell elements grouped into rectangular panels. In the simplest case, the panels are modeled with isotropic constitutive properties. Alternatively, virtual stiffeners can be incorporated into the panel stiffness matrix to achieve the effect of a blade-stiffened panel (see Figure 7). Each panel can have variables to control panel thickness, stiffener thickness, height, and pitch.

The structural model predicts stress and buckling limits, which can be used as constraints in an optimization problem. Rather than constrain the structural failure on an element-by-element basis, we aggregate the failure constraints using the Kreisselmeier–Steinhauser (KS) function. The KS is a conservative approximation of the maximum, meaning that it will overestimate the failure of the structure and provide us with a conservative design. Without constraint aggregation, there would be thousands of structural constraints, each of which would require an adjoint calculation. To make the adjoint approach worthwhile, it is necessary to have far fewer function outputs than design variables [32, Sec. 6.7].

3.3 Mission Analysis. In this work, the aircraft’s performance is quantified by the fuel burn throughout a given mission. There are various methods to estimate fuel burn computationally. For preliminary takeoff weight estimation, the fuel burn for a given mission segment is reasonably predicted using fuel fractions extracted from historical data. However, for optimization, it is necessary to derive a formula relating the fuel burn to the actual design of the aircraft. The Bréguet range equation (Equation 3) is a simple yet mathematically sound relationship between the aerodynamic, structural, and propulsion performance of the aircraft:

$$R = \frac{V}{c_T} \frac{L}{D} \ln \frac{W_2}{W_3} \quad (3)$$

In this equation, W_2 and W_3 refer to the aircraft weight at the beginning and end of cruise, respectively. Although Equation 3 bears the name of French aviation pioneer Louis Bréguet, according to Cavcar [33] it was independently derived by Devillers [34] in 1918 and Coffin [35] in 1920. Equation 3 can be further rearranged to calculate fuel burn as follows:

$$\frac{W_2}{W_3} = \exp \left(\frac{c_T R D}{V L} \right) \quad (4)$$

This equation succinctly relates the three dominant disciplines affecting fuel burn, enabling the optimizer to balance them appropriately. However, due to the stated assumptions, Equations 3 and 4 apply specifically to a cruise-climb flight mode, in which altitude steadily increases to enable the constant L/D assumption.

For a more general approach to the range and fuel burn estimation, the MACH framework contains a module called pyMissionAnalysis. Liem et al. [16] created pyMissionAnalysis to enable surrogate-based mission analysis within the context of an aerosturctural optimization problem similar to the one we are considering here. More details on the approach used are given in their paper. Although the basic function of pyMissionAnalysis remains the same, we made significant changes to improve its generality

and practicality. Initially, the code was written with internal surrogate models for the aerodynamics (C_L , C_D , and C_{M_y}). This approach required the creation of aerodynamic data sets with respect to altitude, Mach number, angle of attack, and tail angle at every optimization iteration. To make the code more general, we replaced the internal surrogate model with a set of callback functions through which the user can provide aerodynamic and engine data to pyMissionAnalysis. Derivatives of the functions of interest with respect to external design variables are also supported in the code. Derivatives in pyMissionAnalysis are computed using automatic differentiation to achieve machine precision.

In pyMissionAnalysis, the various mission segments are broken up into integration intervals. The fuel burn, distance, and elapsed time for each interval are computed using integral equations. The states of the mission model system are the weights at the interval endpoints. A solution to the nonlinear system is obtained by driving the weight differences between endpoints of consecutive intervals to zero. As in Liem et al. [16], a line-search stabilized Newton’s method is used to solve the nonlinear system, and the Jacobian is calculated using finite differences. For our purposes in this paper, the solver is set up to perform in the following manner. The user or optimizer provides the solver with a fixed weight, initial fuel weight, and cruise altitude. The solver converges the residuals to zero to reach a valid state for the prescribed inputs. The outputs of the solver are the range, duration, and fuel burn throughout the mission. Incidentally, the input fuel weight and the output fuel burn can differ if the aircraft starts with enough fuel to complete the given mission. The optimizer can choose inputs that lead to an impractical solution with this setup. For example, the solution will be invalid if the drag at a given altitude exceeds the maximum available thrust. Therefore, in addition to the standard outputs, pyMissionAnalysis computes slack functions that can be used to force a valid solution. For the climb segments, the slack function at each node along the mission profile is the actual climb rate minus the required residual climb rate. The slack function is the available thrust minus the required thrust for the cruise and descent segments. In an optimization problem, these slack functions are constrained to be greater than zero.

For the mission profile depicted in Figure 3 the formula to compute fuel burn is

$$W_{\text{fuel}} = W_5 \left(\frac{W_0}{W_1} \frac{W_1}{W_2} \frac{W_2}{W_3} \frac{W_3}{W_4} \frac{W_4}{W_5} - 1 \right) \quad (5)$$

The final weight of the aircraft, W_5 , is the sum of the operating empty weight (OEW), payload, and reserve fuel. It varies during the optimization due to structural sizing and wing shape changes. The fuel fractions in Equation 5 can be calculated in various ways. At the most basic level, they can be taken from historical data. In this work, the takeoff (W_0/W_1) and landing (W_4/W_5) fuel fractions are fixed at 0.98 and 0.995, respectively. The climb and descent fuel burn can also be represented with fixed values. Brooks et al. [9], for example, the climb and descent fuel fractions are implicitly set to unity. Equation 4 is used to approximate fuel burn over the entire mission range. This approximation is appropriate for medium to long-haul flights (Figure 8) and is often used in the literature. Alternatively, the cruise and descent fuel fractions can be set to historical values. The cruise fuel burn can be computed based on a restricted range corresponding to the estimated distance covered in cruise flight.

For a more general solution, the fuel burn and distance of the climb, cruise, and descent segments can be integrated using pyMissionAnalysis. For example, the data for Figure 8 was generated using 31 intervals for climb, 15 intervals for cruise, and 18 intervals for descent. The climb and descent profiles are split into subregions characterized by accelerated (decelerated), constant calibrated airspeed (CAS), and constant Mach flight (Figure 3). The integration intervals are apportioned to the various subregions to achieve an acceptable resolution across the mission profile. The mission is solved simultaneously by driving the weight differences

between endpoints of consecutive intervals to zero. Thousands of aerodynamic analyses are required to converge to a valid solution, and thousands more are necessary to calculate sensitivities. The cost of using CFD for these aerodynamic analyses would be exorbitant. Liem et al. [16] used CFD to generate a surrogate model of aerodynamic properties at each optimization iteration. The surrogate model was then used to efficiently process the aerodynamic analyses required to solve the mission problem. In this work, we use a conceptual-level aerodynamic model provided by pyConcept to reduce the computational cost of the mission analysis.

As stated in the introduction, one of the aims of this study is to evaluate the impact of using different fuel burn computation methods on the optimized wing design. The four methods considered are listed in Table 4. Whenever three values are given, separated by slashes, they correspond to the nominal, long-range, and high-speed missions of Table 3. For all methods, pyMissionAnalysis uses aerodynamic data from pyConcept. In contrast, the Bréguet equation is always used in conjunction with high-fidelity aerostuctural solutions from MACH. Thus, the Hybrid method combines low-fidelity data for climb and descent and high-fidelity data for cruise. The fixed fuel fractions and ranges for the Cruise-Bréguet method are the values calculated for the baseline configuration using the Full Mission method. It is worth noting that none of these methods in and of themselves are novel contributions. Some of them are frequently used in the literature and have already been demonstrated in this paper. For example, the Full-Bréguet method is used in Brooks et al. [9], and the Full Mission method was used to analyze the missions for Figure 8. The unique contribution of this study lies in comparing the methods to each other, with a particular focus on how they impact the final design in a wing optimization problem.

3.4 Engine Model. The engine performance is represented using a surrogate model built from engine data of thrust and fuel consumption with respect to true airspeed, altitude, and temperature. We use a surrogate model from the Surrogate Modeling Toolbox (SMT)⁴ called regularized minimal-energy tensor-product splines (RMTS) [36]. SMT is especially suited to gradient-based optimization because it provides analytic gradients of the functions of interest with respect to the independent variables. The available thrust at a given flight condition is throttled to the value needed to satisfy minimum residual climb limits (in climb) or offset drag exactly (in cruise). The relationship between engine fuel consumption and throttle setting is modeled as a quartic polynomial based on engine data. All engine data was provided by Embraer.

4 Mission Fuel Burn Trade Study

It is instructive to visualize the variation in the relationship between the climb and cruise segments with respect to mission range, payload, and cruise altitude. Figure 8 was created by computing the fuel burn over the climb and cruise segments for missions ranging from 300 to 2000 nm with varying payloads and cruise altitudes. The data was generated using the mission analysis, engine model, and low-fidelity aerodynamic model described in Section 3, applied to the R-jet aircraft. The first two rows of Figure 8 show the ratios of climb fuel to cruise fuel and climb range to cruise range, respectively. As expected, both ratios increase exponentially as the total mission range decreases. Also, the ratios increase with increasing payload and cruise altitude. At any given data point, the magnitude of the fuel ratio is more than twice that of the range ratio, confirming that the fuel burn per mile is greater in climb than in cruise. The inverse of the rate of fuel burn per distance covered, known as the specific range, is plotted in the final row of Figure 8. Here again, we see that the specific range in cruise is more than twice that achieved in climb. In these plots, the data corresponding to the R-jet payload and cruise altitude are highlighted in blue. From this preliminary study, it is apparent that it

is critical to include the climb fuel burn in the objective function for the 600 nm nominal mission and especially the 300 nm high-speed mission. In Section 5, we show how this modeling decision impacts the optimized design.

5 Simple Wing Optimization

In this section, we compare three different methods of mission analysis and evaluate their impact on the optimization of the R-wing configuration. We compare multipoint optimizations of the Cruise-Bréguet and Hybrid methods (considering the three missions of Table 3).

5.1 Optimization Problem. The R-wing optimization problem is detailed in Table 5. The objective is to minimize the aggregated fuel burn defined by Equation (1) augmented with operating empty weight to create a multi-objective problem. The objective function is

$$\beta \bar{W}_{\text{fuel}} + (1 - \beta) \text{OEW} \quad (6)$$

The parameter β varies between 0.5 and 1.0 to generate a Pareto front that illustrates the trade-off between aircraft weight and fuel burn. The Pareto front was not extended below $\beta = 0.5$ because it was apparent from the curve's trend that further reductions in structural weight would incur an unacceptable increase in fuel burn. We also experiment with three different combinations of geometric design variables. This brings the final tally of optimization runs to 24: two mission analysis methods, four points along the Pareto front, and three different sets of design variables.

For each optimization problem, there are four different high-fidelity analysis points, each of which has a design variable to control the angle of attack. We consider the following three combinations of geometric variables:

- (1) Only twist variables (at four spanwise stations)
- (2) Twist and planform variables (one span, one sweep, and five chord scaling)
- (3) Twist, planform, and local shape variables

The structure is parametrized with the blade-stiffened panels described in Section 3.2. The number of structural design variables for each case remains the same. Fuel load traction variables are used to vary the tractions on the skin panels so that, in aggregate, they impart a load equal to the total fuel mass variable. In turn, the total fuel mass variable is constrained to be consistent with the actual fuel burn of the given mission for the current iterate. For the optimizations using the Hybrid mission analysis, there are two variables corresponding to the initial and final weights of the climb and descent segments of the three missions. For these studies, we do not allow the cruise altitude to vary from 36,000 ft.

Each mission is constrained to achieve its specified range. The high-fidelity analysis point for each mission is constrained to generate enough lift to support the mid-cruise weight (the average of W_2 and W_3). Yield stress and buckling constraints are evaluated under the loads imposed by a 2.5g pull-up maneuver at Mach 0.734 and 15,000 ft. This design point also carries a payload of 13,000 kg and a full fuel load of 12,900 kg. Yield stress failure constraints are aggregated over the upper and lower skins separately. Buckling constraints are aggregated over the ribs and spars and separately over the upper skin. The geometry is constrained, so the thickness cannot decrease at 1% and 99% chord. Additionally, the thickness cannot decrease below 80% of the original value at 60% chord. The chord variables are constrained to decrease monotonically from root to tip. For the case with shape variables, constraints are applied to the FFD points at the leading and trailing edges to ensure that they move in equal and opposite directions to prevent shearing twist. We also constrain the planform area from decreasing when the planform variables are active. The Hybrid mission analysis method uses constraints to force the mission slack functions to be greater than or equal to zero (see

⁴<https://github.com/SMTorg/smt>

Table 4 Four methods for calculating the fuel burn and range of a mission.

	Full-Bréguet	Full Mission	Cruise-Bréguet	Hybrid
W_0/W_1	0.98	0.98	0.98	0.98
W_1/W_2	1.0	pyMissionAnalysis	0.977/0.976/0.977	pyMissionAnalysis
W_2/W_3	Bréguet	pyMissionAnalysis	Bréguet	Bréguet
W_3/W_4	1.0	pyMissionAnalysis	0.993/0.993/0.992	pyMissionAnalysis
W_4/W_5	0.995	0.995	0.995	0.995
Climb range (nm)	0	pyMissionAnalysis	110/116/105	pyMissionAnalysis
Cruise range (nm)	600/1000/300	pyMissionAnalysis	373/769/67	pyMissionAnalysis
Descent range (nm)	0	pyMissionAnalysis	117/115/128	pyMissionAnalysis

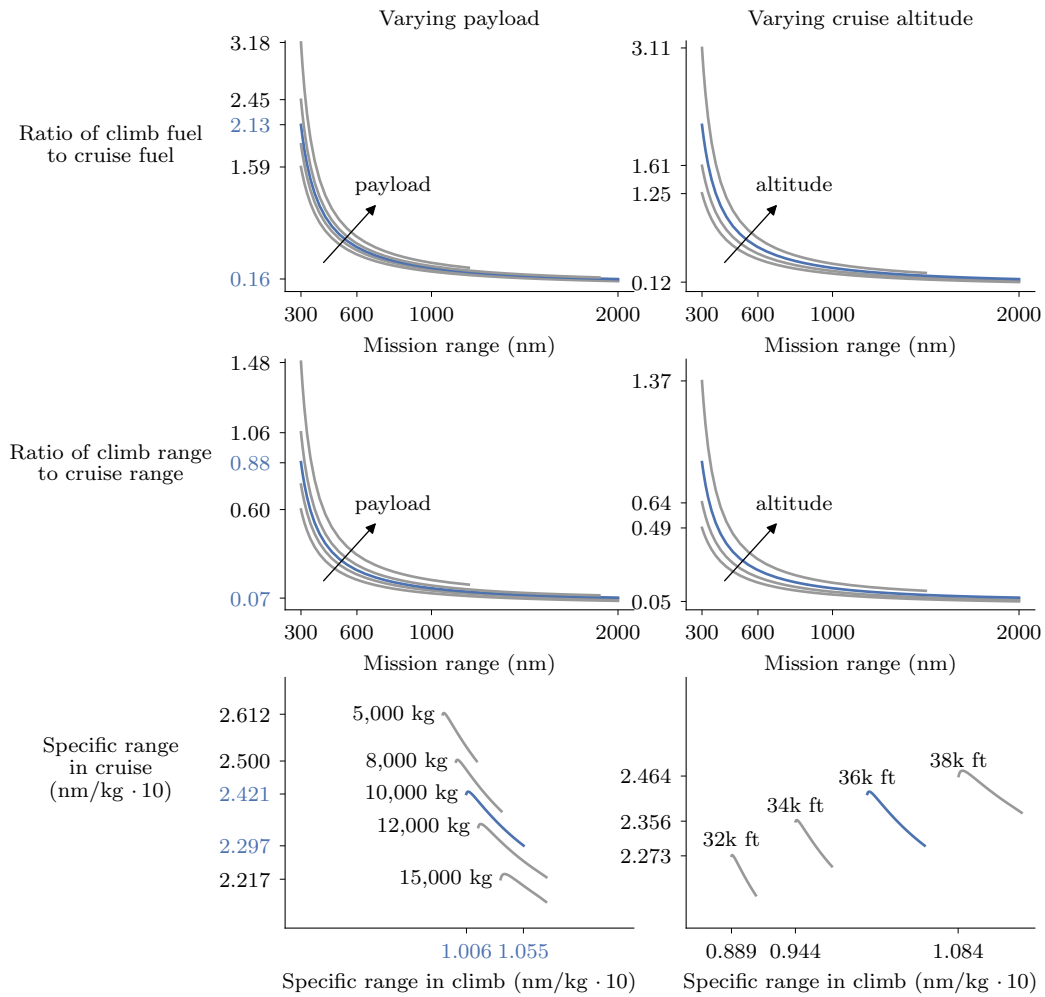


Fig. 8 The ratio of climb fuel burn to cruise fuel burn grows exponentially as mission range decreases. The data corresponding to the R-jet aircraft description is highlighted in blue.

Table 5 Summary of the full R-wing optimization problem. The quantities for each design variable correspond to the green curve in Figure 9.

		Quantity
minimize with respect to	$\beta \bar{W}_{\text{fuel}} + (1 - \beta) \text{OEW}$	1
	Angle of attack	4
	Twist	4
	Planform variables (span, chord, sweep)	7
	Sectional shape	128
	Structural sizing	356
	Panel lengths	146
	Fuel load tractions	108
	Total fuel mass	4
	Mission fuel weights	12
subject to	Range constraints	3
	Trim constraints ($L = W$)	4
	Structural failure constraints	4
	Planform area cannot decrease	1
	Wing geometric constraints	76
	Miscellaneous mission constraints	159
	TACS linear constraints	420
	TACS nonlinear constraints	258
	Fuel load constraints	4

Section 3.3). The linear constraints in TACS consist of adjacency constraints to prevent significant differences in thickness between adjacent panels. The nonlinear constraints in TACS include compatibility constraints for the panel lengths and fuel tractions. Finally, as mentioned previously, each mission has a total fuel mass variable that must be constrained to match the fuel burn of the current iterate.

5.2 Results. Figure 9 shows the two sets of Pareto curves generated for the wing-only optimization. The design variables and constraints for each of the red, blue, and green curves are given in the final three columns of Table 5. Each Pareto front is created by varying β between 0.5 and 1. As expected, adding design variables to the problem shifts the Pareto front to the lower-left-hand corner, signifying overall improvement in the design. Most of the benefit of additional geometric freedom is reduced fuel burn, especially for higher values of β . Impressively, there is roughly a 1-2% reduction in fuel burn between the Pareto fronts.

Each point along the Pareto front is accompanied by a scaled outline of the planform and a number referring to the aspect ratio of the optimized wing. Interestingly, when only cruise fuel burn is considered in the optimization objective, the aspect ratios do not increase significantly beyond the baseline geometry, even when $\beta = 1$. However, when the full mission fuel burn (including climb and descent) is considered, the aspect ratios for higher β values increase significantly. The plots in Figure 9 highlight these differences. The right-hand plot shows the expected trend that the aspect ratio should increase to decrease fuel burn.

For a regional jet, the mass of fuel burned over a typical mission is on par with the mass of the wingbox structure. Therefore, the fuel burn reduction resulting from a decrease in wingbox mass is closer to that achieved through aerodynamic enhancements than for an aircraft with a longer mission. This seems to be why accounting for the fuel burn over the entire mission causes an increase in aspect ratio for $\beta = 1$. When only the cruise segment is considered, the benefit of increasing the aspect ratio does not outweigh the penalty in fuel burn due to the increase in structural mass required to support a higher aspect ratio. This result validates our use of mission analysis for the full configuration optimization study. Perhaps for a larger aircraft, constant fuel fractions would be sufficient, but for a regional jet, the gains made in fuel burn reduction over climb and descent matter.

One possible explanation for the increased emphasis on drag reduction in the Hybrid method results is that the low-fidelity model used in the mission calculations over-predicts the possible drag reduction on the climb and descent segments. On the contrary, post-optimization high-fidelity analysis of points along the climb and descent profiles yields more significant drag reductions than were predicted by the low-fidelity analysis (Figure 10). Thus, it is

more likely that using the low-fidelity aerodynamic analysis in the mission calculations yields a conservative result for the optimized design.

In wing design, the optimal aspect ratio depends on the trade-off between structural weight and fuel burn. The balance between the structural weight and fuel burn can be adjusted explicitly by controlling their relative importance in a weighted average objective function. For instance, in our Pareto front studies, the wings optimized for minimum fuel burn ($\beta = 1$) had higher aspect ratios than those with more emphasis on structural weight ($\beta = 0.5$). On the other hand, the optimal aspect ratio is implicitly dependent on the relative magnitudes of the structural and fuel weights, specifically the variable quantities in the optimization. For a short-haul regional jet, the fuel and the wing structure have weights of similar magnitude. Thus, the assumptions built into the fuel burn calculation can significantly impact the balance between fuel weight and structural weight and, by extension, the aspect ratio of the optimized wing. Modeling the climb segment, and including its fuel burn in the objective function, increases the incentive for the optimizer to reduce fuel burn through drag reduction.

6 Full Aircraft Optimization

Now that we have demonstrated the value of including mission analysis in optimizing a simple wing geometry, we will move on to optimizing the wing of the full R-jet configuration. The primary aim of this optimization problem is to see how the optimizer alters the design of the original regional jet. Because the baseline wing is already a “good” design, significant differences between the baseline and optimized designs indicate either a shortcoming of the optimization problem or a previously unattainable improvement made possible with the MDO approach. We start by sizing the wingbox structure to achieve minimum mass while satisfying the baseline configuration’s structural constraints. In this way, structural and fuel weight comparisons between the baseline and optimized designs are fair. The full optimization problem includes variables to modify the twist distribution, cross-sectional shape, and planform of the wing, in addition to the structural sizing variables. The horizontal tail can also change in size to match planform changes in the wing.

As an intermediary step, we also optimize the wing without planform variables. To differentiate between them, we designate the reduced problem S+T (shape and twist), while the full problem is labeled S+T+P (shape, twist, and planform). The result of the S+T problem informs our assessment of the success of the S+T+P optimization. While we fully expect the S+T+P optimized design to perform better than the baseline, it would be difficult to determine whether the improvements were due to the merits of MDO or to missing constraints in the optimization problem. The result

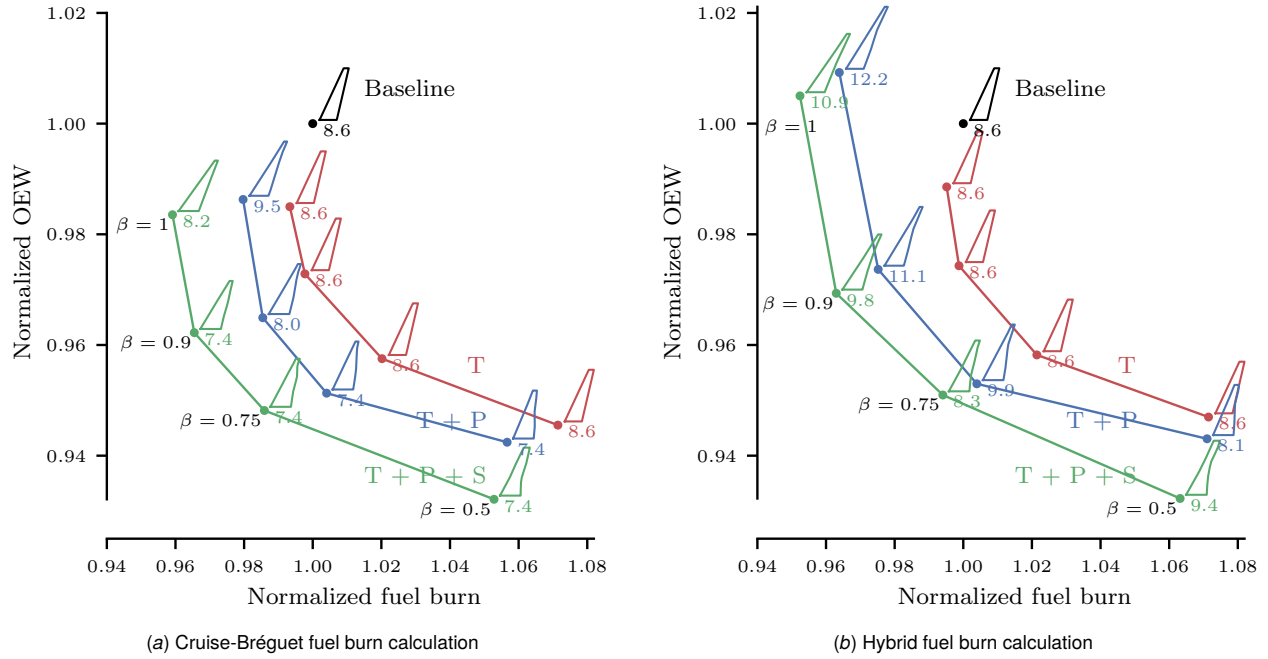


Fig. 9 Pareto fronts from optimizations using different methods of fuel burn calculation.

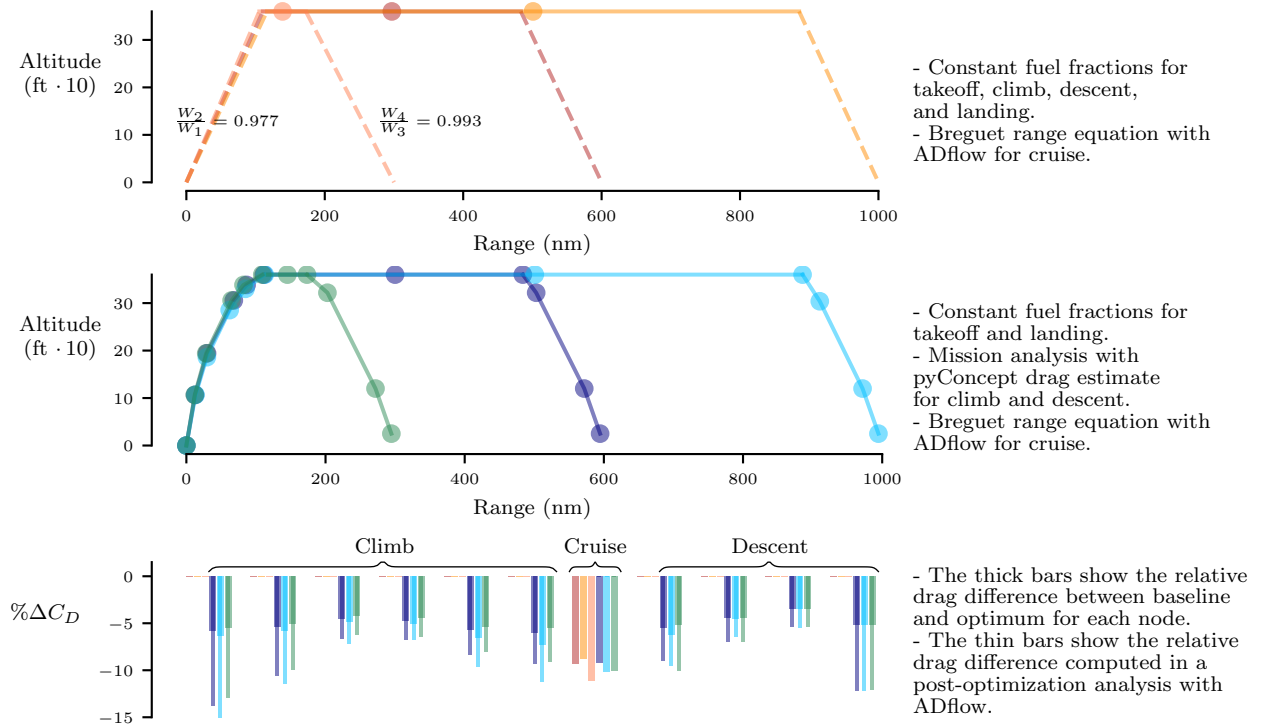


Fig. 10 The low-fidelity aerodynamic analysis used in pyMissionAnalysis underestimates the drag reduction at several points along the climb and descent profiles.

of the S+T optimization provides a clearer picture of the benefit of simultaneously optimizing the wing's structure, planform, and cross-sectional shape.

For the S+T+P problem, the tail size is constrained to maintain the tail volume coefficient of the baseline design. Including a tail scaling variable and a tail sizing constraint in the optimization problem is uncommon in the literature, and the effects are not obvious. The last case presented in this section is a control for the tail sizing experiment and does not allow the horizontal tail to scale. In all other respects, it is identical to the S+T+P problem.

6.1 Tail Sizing Constraint. Adjustments to the wing planform can have global consequences on the design of the aircraft. For instance, we must ensure that the wing's planform does not change such that the tail is underpowered to counter the wing moment. This could occur due to changes in the location of the mean aerodynamic chord or the overall area of the wing. Raymer [30] suggests using a tail volume coefficient to match the moments produced by the tail and the wing. This parameter is purely geometrical, so adding it as a function in pyConcept was straightforward. The tail volume coefficient is defined as

$$c_{\text{tail}} = \frac{L_{\text{tail}} S_{\text{tail}}}{\bar{c} S_{\text{wing}}} \quad (7)$$

where

$$L_{\text{tail}} = \bar{x}_{\text{tail}} - \bar{x}_{\text{wing}}$$

and \bar{x} is the quarter-chord position of the mean aerodynamic chord (\bar{c}) of the lifting surface. Each of the parameters used in the expression for c_{tail} is updated in pyConcept based on changes in the FFDs of the wing and the tail. Additional geometric variables are assigned to the FFD enclosing the horizontal tail to allow it to scale up or down to match the changes in the wing planform.

6.2 Optimization Problem. The full optimization problem, corresponding to the S+T+P case, is listed in Table 6. The optimization problem is very similar to the problem solved in Section 5, so here we will only mention some differences. The first significant difference is that the objective function is simply the composite fuel burn rather than a weighted average of fuel burn and OEW. The geometric parametrization is also slightly different for the R-jet. The twist distribution is controlled at six spanwise stations, whereas the chord can only scale at the mid-span kink, the wingtip, and the tip of the winglet. The tail rotates to trim the aircraft and scales to match changes in the planform (following the tail volume coefficient constraint). We include a constraint to ensure a 30% margin to buffet in cruise flight for this problem. The buffet constraint is formulated based on the method of Kenway and Martins [37] and is applied at the nominal cruise flight condition under a 1.3g load. The tail volume coefficient is constrained to be greater than or equal to the baseline value.

6.3 Results. The percentage differences between the optimized and baseline designs are listed in Table 7. Fuel burn decreases across all missions, with the most significant percentage difference in fuel burn coming from the long-range mission. The S+T design reduces fuel burn by 1.8% compared to the baseline. With the addition of planform variables, the optimized design achieves an additional 1.8% reduction in the objective, double that of the S+T design. The structural weight of the S+T+P design is roughly 5% greater than the baseline, whereas the S+T design reduces the weight by slightly more than 8%. The increase in weight on the S+T+P wing is necessary to support an increased aspect ratio of more than 25% greater than the baseline design. Interestingly, the lift-to-drag ratio increases for nominal and long-range missions but decreases for the high-speed mission. This is because longer-range missions burn more fuel and therefore offer more fuel in terms of fuel burn reduction than is lost on high-speed missions.

Table 6 R-jet optimization problem

	Quantity
minimize	\bar{W}_{fuel}
with respect to	Angle of attack
	Tail rotation
	Twist
	Span
	Sweep
	Chord scaling
	Tail scaling
	Sectional shape
	Structural sizing
	Panel lengths
	Fuel load tractions
	Total fuel mass
	Mission fuel weights
	Total number of design variables
subject to	Range constraints
	Trim constraints ($L = W, C_{M,y} = 0$)
	Structural failure constraints
	Planform area cannot decrease
	Tail volume coefficient constraint
	Wing geometric constraints
	Buffet onset constraint (1.3g)
	Miscellaneous mission constraints
	Structural sizing adjacency constraints
	Panel length consistency constraints
	Fuel traction consistency constraints
	Total fuel mass constraints
	Fuel volume constraints
	Total number of design constraints

Table 7 Percentage difference between baseline and optimized R-jet designs.

	S+T	S+T+P	S+T+P (fixed tail)
<i>Fuel burn</i>			
Nominal	-1.9	-3.6	-3.3
Long-range	-2.6	-4.8	-4.5
High-speed	-0.7	-1.9	-1.9
Combined	-1.8	-3.6	-3.4
<i>Mass</i>			
OEW	-1.1	+0.7	+0.5
Wing	-8.1	+4.9	+3.8
<i>L/D</i>			
Nominal	+3.1	+6.7	+5.9
Long-range	+3.6	+8.0	+7.2
High-speed	-1.9	-1.6	-1.4
<i>Geometry</i>			
Aspect ratio	0.0	+26.5	+28.8
Span	0.0	+12.5	+13.5
Sweep	0.0	-24.2	-15.2

Airfoil slices and C_p distributions of the baseline, S+T, and S+T+P designs are shown in Figure 11. The most noticeable change to the S+T airfoils is decreased thickness-to-chord ratio, especially on the outboard wing. The S+T+P airfoils feature a decrease in the twist and a more pronounced aft camber than the baseline. Both optimized designs have a more gradual pressure rise at the nominal design point, but a shock that did not exist on the baseline wing appears on these optimized wings. Remarkably, the C_p distributions for the long-range design point are similar for the three designs.

Spanwise distributions of lift, twist, and t/c are plotted with respect to normalized span in Figure 12. The lift distribution for the S+T design is nearly identical to that of the baseline wing. Since it has a longer span, the S+T+P design can generate less lift on the outboard wing, reducing the bending moment caused by tip loads. In the plot of twist distributions, the effects of passive load alleviation at the maneuver condition are readily apparent. The bend-twist coupling in the structure produces a moment to untwist the wing when deflected under the heavy 2.5g load. As observed in the airfoil slices, the plot of t/c shows a substantial reduction in thickness in the outboard wing on both optimized designs.

The most striking differences between the baseline and S+T+P designs are the aspect ratio increase and wing sweep decrease, as shown in Figure 13. Basic aerodynamic theory tells us that induced and wave drag vary inversely with span and sweep, respectively. However, both span and sweep are tightly coupled with the structural response of the wing as well. Any increase in span or sweep generally requires a heavier wing structure to support the increased moment arm. To determine the correct trade-off between span and sweep, it is critical to model the wing aerostructurally. In this case, the optimizer increases the span to reduce induced drag at the cost of a heavier wing. At the same time, the decrease in wing sweep lightens the burden on the wing while possibly degrading the high-speed performance of the wing (as evidenced by the shocks shown on the high-speed design point in Figure 11). The right side of Figure 13 shows the deflected state of the optimized wings at cruise and maneuver conditions.

When the scaling of the horizontal tail is an active design variable, the optimizer chooses to shrink it to reduce drag. Since the wing area cannot decrease, Equation 7 dictates that the tail area can only decrease if the wing sweep is reduced. With the horizontal tail area fixed, the optimizer reduces the wing sweep, but not as much as in the former case. In the case without a fixed tail area, the optimizer is degrading the wing's performance slightly to reap the benefits of a smaller horizontal tail which leads to better overall performance. Whereas the designer might be reluctant to sacrifice wing performance and therefore arrive at a suboptimal overall design, the optimizer has no such inhibitions and finds a proper trade-off between wing performance and tail size. The difference in the sizes of the horizontal tails can be seen in Figure 13.

Contours of the structural failure and buckling criteria, skin thickness, and aeroelastic deflection for the baseline and S+T+P designs are shown in Figure 14. The panel thickness on the upper and lower skins increases to support the longer wingspan.

7 Conclusion

In Section 5, we demonstrated that different methods of calculating fuel burn can impact the optimized design. We experimented with a method for mission analysis that combined low-fidelity aerodynamic analyses along the climb and descent segments with a high-fidelity aerostructural analysis to represent the mid-cruise point. With this hybrid method, the fuel burn on the climb and descent segments is included in the objective function and depends on the geometric parametrization. For short-haul missions, where the aircraft burns a significant portion of the total fuel burn in climb, the correct trade-offs are more likely to be achieved with this approach.

In Section 6, we test the merits of the MACH framework by optimizing an Embraer regional jet. The wing optimized with shape,

twist, and planform variables burns 3.6% less fuel than the baseline design and 1.8% less fuel than a wing optimized with only shape and twist variables. When all the variables are included, the wingspan increases substantially, and the wing sweep is reduced compared to the baseline. The significant differences between the baseline and optimized wings showcase the advantage of simultaneously optimizing all variables while considering the aerostructural coupling of the wing. As mentioned previously, both span and sweep are tightly coupled with the structural response of the wing as well. To determine the correct trade-off between span and sweep, it is critical to model the wing aerostructurally.

The application of MDO to authentic commercial aircraft is unique. While the design problem presented herein is a simplified version of the actual aircraft design problem, it includes many of the most relevant design considerations. Part of this work's value is demonstrating the feasibility of applying MDO to a design problem at a commercial aircraft company. Additionally, our results show noticeable differences between the optimized and baseline designs. The wing design is likely influenced by some constraints and requirements neglected in this study. Similarly, it is possible that improving the model accuracy would change the numerical performance of the optimal result. However, despite such limitations, these results indicate that the simultaneous design of wing-box structure, wing planform, and wing cross-sectional shapes will yield a different wing design than when each is designed separately.

8 Acknowledgments

The authors would like to acknowledge Embraer for the funding and the technical support of this project. Special thanks to the following individuals: Tarik Hadura Orra for his support on the mission requirements and constraints; Yvan Bovolenta Murta and Fabio Ribeiro Soares da Cunha for their support on structural layout and model, structural constraints, and structural results analysis; Raphael Felipe Gama Ribeiro for his support on engine data; and Rodrigo Felix de Souza for his help with the aircraft outer mold line, aerodynamic constraints, and aerodynamic results analysis.

References

- [1] Grossman, B., Gurdal, Z., Strauch, G. J., Eppard, W. M., and Haftka, R. T., 1988, "Integrated Aerodynamic/Structural Design of a Sailplane Wing," *Journal of Aircraft*, **25**(9), pp. 855–860.
- [2] Chittick, I. R. and Martins, J. R. R. A., 2008, "Aero-Structural Optimization Using Adjoint Coupled Post-Optimality Sensitivities," *Structures and Multidisciplinary Optimization*, **36**, pp. 59–70.
- [3] Jansen, P., Perez, R. E., and Martins, J. R. R. A., 2010, "Aerostructural Optimization of Nonplanar Lifting Surfaces," *Journal of Aircraft*, **47**(5), pp. 1491–1503.
- [4] Cavagna, L., Ricci, S., and Riccobene, L., 2011, "Structural Sizing, Aeroelastic Analysis, and Optimization in Aircraft Conceptual Design," *Journal of Aircraft*, **48**(6), pp. 1840–1855.
- [5] Cavagna, L., Ricci, S., and Travaglini, L., 2011, "NeoCASS: An integrated tool for structural sizing, aeroelastic analysis and MDO at conceptual design level," *Progress in Aerospace Sciences*, **47**(8), pp. 621–635.
- [6] Elham, A. and van Tooren, M. J. L., 2016, "Coupled adjoint aerostructural wing optimization using quasi-three-dimensional aerodynamic analysis," *Structural and Multidisciplinary Optimization*, **54**(4), pp. 889–906.
- [7] Kenway, G. K. W. and Martins, J. R. R. A., 2014, "Multipoint High-Fidelity Aerostructural Optimization of a Transport Aircraft Configuration," *Journal of Aircraft*, **51**(1), pp. 144–160.
- [8] Kroll, N., Abu-Zurayk, M., Dimitrov, D., Franz, T., Führer, T., Gerhold, T., Görtz, S., Heinrich, R., Ilic, C., Jepsen, J., Jägersküpper, J., Kruse, M., Krumbain, A., Langer, S., Liu, D., Liepelt, R., Reimer, L., Ritter, M., Schwöppe, A., Scherer, J., Spiering, F., Thormann, R., Togiti, V., Vollmer, D., and Wendisch, J.-H., 2016, "DLR project Digital-X: towards virtual aircraft design and flight testing based on high-fidelity methods," *CEAS Aeronautical Journal*, **7**(1), pp. 3–27.
- [9] Brooks, T. R., Kenway, G. K. W., and Martins, J. R. R. A., 2018, "Benchmark Aerostructural Models for the Study of Transonic Aircraft Wings," *AIAA Journal*, **56**(7), pp. 2840–2855.
- [10] Mader, C. A., Kenway, G. K., Martins, J. R. R. A., and Uranga, A., 2017, "Aerostructural Optimization of the D8 Wing with Varying Cruise Mach Numbers," *18th AIAA/ISSMO Multidisciplinary Analysis and Optimization Conference*, American Institute of Aeronautics and Astronautics, doi: [10.2514/6.2017-4436](https://doi.org/10.2514/6.2017-4436).

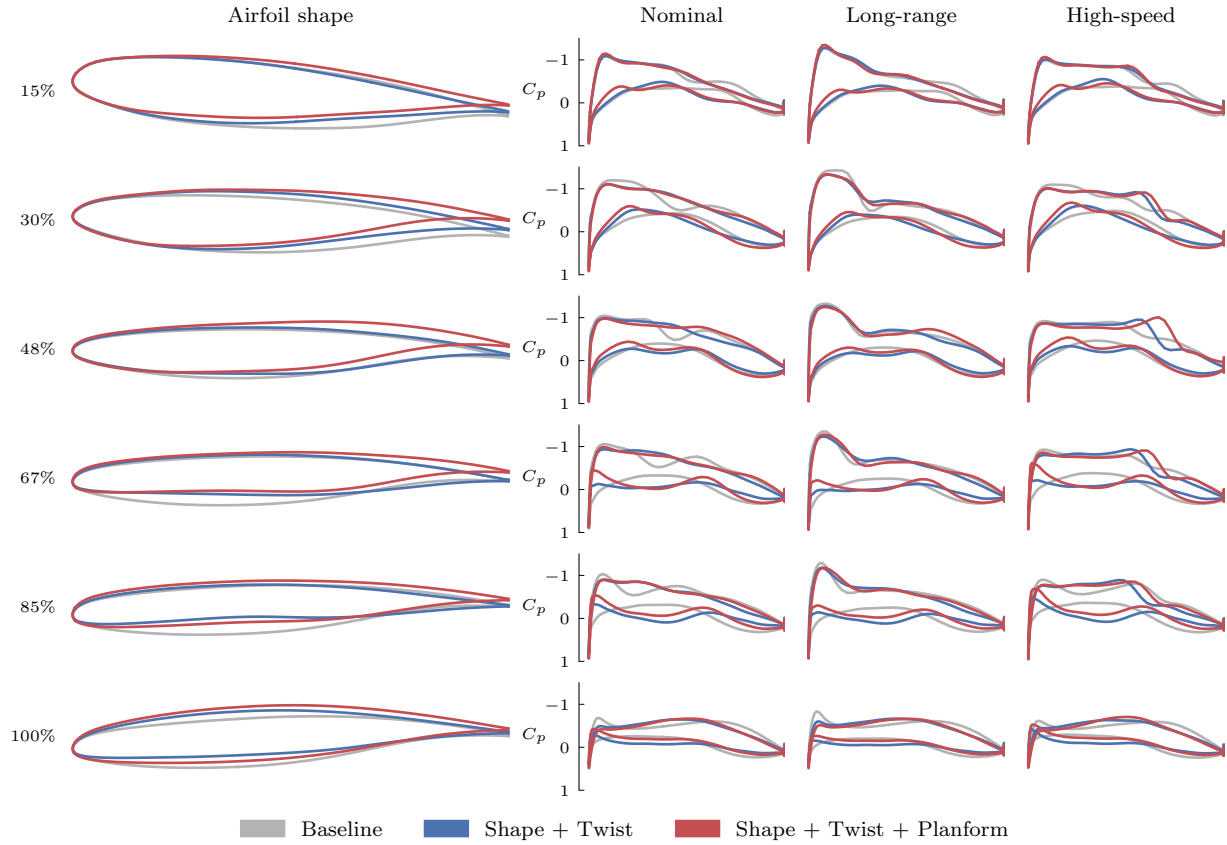


Fig. 11 Comparison of airfoils and C_p distributions for different cases.

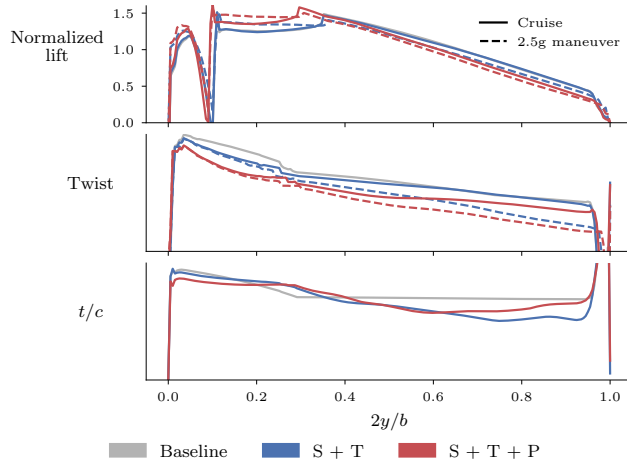


Fig. 12 Comparison of spanwise lift, twist, and t/c distributions for different cases.

- [11] Brooks, T. R., Martins, J. R. R. A., and Kennedy, G. J., 2019, "High-fidelity Aerostructural Optimization of Tow-steered Composite Wings," *Journal of Fluids and Structures*, **88**, pp. 122–147.
- [12] Brooks, T. R., Martins, J. R. R. A., and Kennedy, G. J., 2020, "Aerostructural Trade-offs for Tow-steered Composite Wings," *Journal of Aircraft*, **57**(5), pp. 787–799.
- [13] Bons, N. P., Martins, J. R. R. A., Mader, C. A., McMullen, M., and Suen, M., 2020, "High-fidelity Aerostructural Optimization Studies of the Aerion AS2 Supersonic Business Jet," *Proceedings of the AIAA Aviation Forum*, doi: [10.2514/6.2020-3182](https://doi.org/10.2514/6.2020-3182).
- [14] Drela, M., 1998, *Frontiers of Computational Fluid Dynamics*, World Scientific, Chap. Pros and Cons of Airfoil Optimization, pp. 363–381.
- [15] Liem, R. P., Kenway, G. K. W., and Martins, J. R. R. A., 2015, "Multimission Aircraft Fuel Burn Minimization via Multipoint Aerostructural Optimization," *AIAA Journal*, **53**(1), pp. 104–122.
- [16] Liem, R. P., Mader, C. A., Lee, E., and Martins, J. R. R. A., 2013, "Aerostructural design optimization of a 100-passenger regional jet with surrogate-based mission analysis," *2013 Aviation Technology, Integration, and Operations Conference*, doi: [10.2514/6.2013-4372](https://doi.org/10.2514/6.2013-4372).
- [17] Lee, H. and Chatterji, G. B., 2010, "Closed-Form Takeoff Weight Estimation Model for Air Transportation Simulation," *10th AIAA Aviation Technology, Integration, and Operations (ATIO) Conference*, Fort Worth, TX, doi: [10.2514/6.2010-9156](https://doi.org/10.2514/6.2010-9156).
- [18] Kenway, G. K. W., Kennedy, G. J., and Martins, J. R. R. A., 2014, "Scalable Parallel Approach for High-Fidelity Steady-State Aeroelastic Analysis and Adjoint Derivative Computations," *AIAA Journal*, **52**(5), pp. 935–951.
- [19] Lambe, A. B. and Martins, J. R. R. A., 2012, "Extensions to the Design Structure Matrix for the Description of Multidisciplinary Design, Analysis, and Optimization Processes," *Structural and Multidisciplinary Optimization*, **46**, pp. 273–284.
- [20] Gill, P. E., Murray, W., and Saunders, M. A., 2007, *User's Guide for SNOPT Version 7: Software for Large-Scale Nonlinear Programming*, Systems Optimization Laboratory, Stanford University, California, 94305-4023, Technical Report.
- [21] Wu, N., Kenway, G., Mader, C. A., Jasa, J., and Martins, J. R. R. A., 2020, "pyOptSparse: A Python framework for large-scale constrained nonlinear optimization of sparse systems," *Journal of Open Source Software*, **5**(54), p. 2564.
- [22] Sederberg, T. W. and Parry, S. R., 1986, "Free-form Deformation of Solid Geometric Models," *SIGGRAPH Comput. Graph.*, **20**(4), pp. 151–160.
- [23] Kenway, G. K., Kennedy, G. J., and Martins, J. R. R. A., 2010, "A CAD-Free Approach to High-Fidelity Aerostructural Optimization," *Proceedings of*

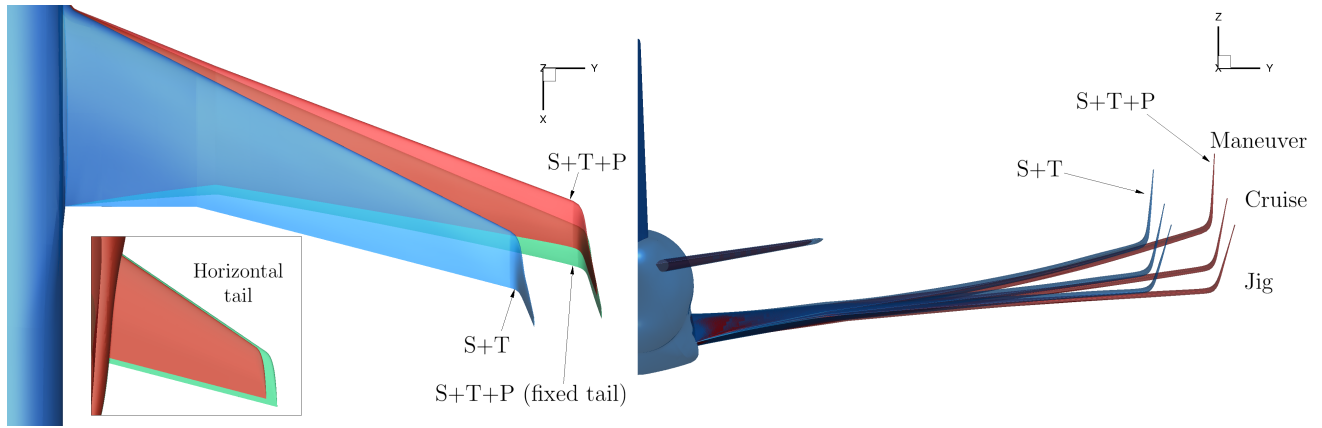


Fig. 13 Wing planforms and deflected shapes for the optimized wings. The S+T wing planform is identical to the baseline wing.

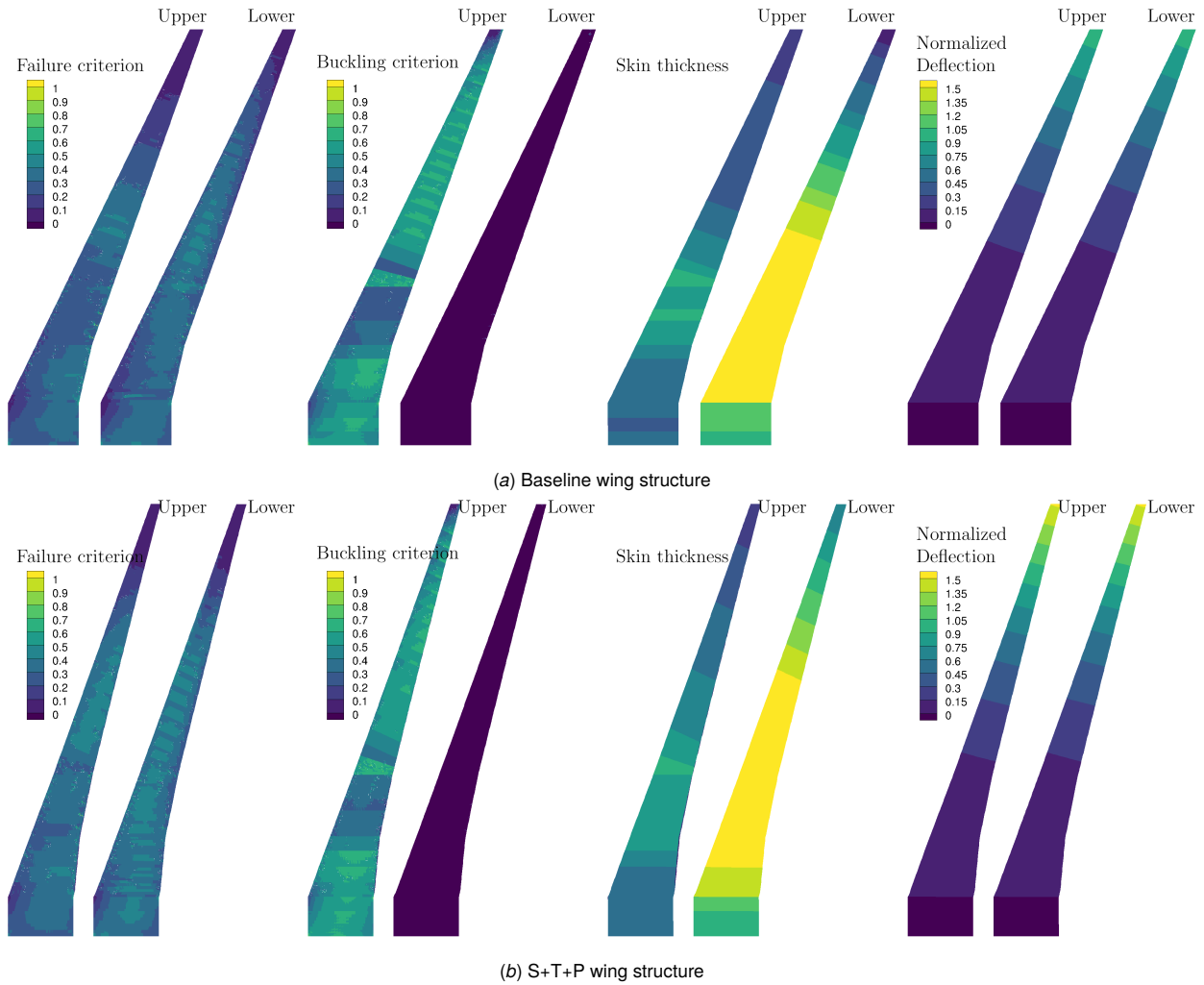


Fig. 14 Comparison of baseline and optimized wingbox structures. The wing deflection is normalized by the maximum tip deflection on the baseline wing.

- the 13th AIAA/ISSMO Multidisciplinary Analysis Optimization Conference, Fort Worth, TX, [Paper No. AIAA 2010-9231](#).
- [24] Secco, N., Kenway, G. K. W., He, P., Mader, C. A., and Martins, J. R. R. A., 2021, "Efficient Mesh Generation and Deformation for Aerodynamic Shape Optimization," *AIAA Journal*, **59**(4), pp. 1151–1168.
- [25] Kenway, G. K. W., Mader, C. A., He, P., and Martins, J. R. R. A., 2019, "Effective Adjoint Approaches for Computational Fluid Dynamics," *Progress in Aerospace Sciences*, **110**, p. 100542.
- [26] Yildirim, A., Kenway, G. K. W., Mader, C. A., and Martins, J. R. R. A., 2019, "A Jacobian-free approximate Newton–Krylov startup strategy for RANS simulations," *Journal of Computational Physics*, **397**, p. 108741.
- [27] Kennedy, G. J. and Martins, J. R. R. A., 2014, "A parallel aerostructural optimization framework for aircraft design studies," *Structural and Multidisciplinary Optimization*, **50**(6), pp. 1079–1101.
- [28] Brown, S. A., 1997, "Displacement Extrapolation for CFD+CSM Aeroelastic Analysis," *Proceedings of the 35th AIAA Aerospace Sciences Meeting*, Reno, NV, AIAA 1997-1090.
- [29] Kennedy, G. J. and Martins, J. R. R. A., 2010, "Parallel Solution Methods for Aerostructural Analysis and Design Optimization," *Proceedings of the 13th AIAA/ISSMO Multidisciplinary Analysis Optimization Conference*, Fort Worth, TX.
- [30] Raymer, D. P., 2012, *Aircraft Design: A Conceptual Approach*, 5th ed., AIAA.
- [31] Kennedy, G. J. and Martins, J. R. R. A., 2014, "A Parallel Finite-Element Framework for Large-Scale Gradient-Based Design Optimization of High-Performance Structures," *Finite Elements in Analysis and Design*, **87**, pp. 56–73.
- [32] Martins, J. R. R. A. and Ning, A., 2021, *Engineering Design Optimization*, Cambridge University Press.
- [33] Cavcar, M., 2006, "Bréguet Range Equation?" *Journal of Aircraft*, **43**(5), pp. 1542–1544.
- [34] Devillers, R., 1918, *La dynamique de l'avion*, Librairie aéronautique.
- [35] Coffin, J. G., 1920, "A Study of Airplane Ranges and Useful Loads," National Advisory Committee for Aeronautics, Tech. Rep. 69.
- [36] Hwang, J. T. and Martins, J. R. R. A., 2018, "A fast-prediction surrogate model for large datasets," *Aerospace Science and Technology*, **75**, pp. 74–87.
- [37] Kenway, G. K. W. and Martins, J. R. R. A., 2017, "Buffet-Onset Constraint Formulation for Aerodynamic Shape Optimization," *AIAA Journal*, **55**(6), pp. 1930–1947.

List of Figures

1	Computational grids for the R-jet configuration.	2
2	Computational grids for the R-wing configuration juxtaposed with the R-jet grids.	2
3	Basic mission profile.	3
4	XDSM diagram of aerostructural mission optimization with MACH.	4
5	Points are extracted from the R-wing and R-jet wings in order to create a basic representation of the geometry in pyConcept.	4
6	On both baseline and optimized designs, the low-fidelity drag polar from pyConcept coincides with the high-fidelity aerostructural result at cruise flow conditions. The error in the low-fidelity method grows as the speed and altitude decrease.	5
7	Representative depiction of smeared stiffness model.	6
8	The ratio of climb fuel burn to cruise fuel burn grows exponentially as mission range decreases. The data corresponding to the R-jet aircraft description is highlighted in blue.	8
9	Pareto fronts from optimizations using different methods of fuel burn calculation.	10
	(a) Cruise-Bréguet fuel burn calculation	10
	(b) Hybrid fuel burn calculation	10
10	The low-fidelity aerodynamic analysis used in pyMissionAnalysis underestimates the drag reduction at several points along the climb and descent profiles.	10
11	Comparison of airfoils and C_p distributions for different cases.	13
12	Comparison of spanwise lift, twist, and t/c distributions for different cases.	13
13	Wing planforms and deflected shapes for the optimized wings. The S+T wing planform is identical to the baseline wing.	14
14	Comparison of baseline and optimized wingbox structures. The wing deflection is normalized by the maximum tip deflection on the baseline wing.	14
	(a) Baseline wing structure	14
	(b) S+T+P wing structure	14

List of Tables

1	R-jet aircraft Specifications	2
2	The R-wing mesh reduces the computational cost of aerostructural analysis by a factor of 1500 when compared with the R-jet overset mesh.	2
3	Mission details	3
4	Four methods for calculating the fuel burn and range of a mission.	8
5	Summary of the full R-wing optimization problem. The quantities for each design variable correspond to the green curve in Figure 9.	9
6	R-jet optimization problem	11
7	Percentage difference between baseline and optimized R-jet designs.	11